AUTOMATED LIGHTLESS CYTOMETRY ON A MICROCHIP WITH ADAPTIVE IMMUNOMAGNETIC MANIPULATION

Ozgun Civelekoglu [a, †], Ningquan Wang [a, †], A K M Arifuzzman [a], Mert Boya [a], A. Fatih Sarioglu [a, b, c, *]

[a] School of Electrical and Computer Engineering, Georgia Institute of Technology, Atlanta, Georgia 30332, USA
[b] Parker H. Petit Institute for Bioengineering and Bioscience, Georgia Institute of Technology, Atlanta, Georgia 30332, USA
[c] Institute for Electronics and Nanotechnology, Georgia Institute of Technology, Atlanta, Georgia 30332, USA

[†] These authors contributed equally to this work.
[*] Correspondence should be addressed to A.F.S. (sarioglu@gatech.edu)

ABSTRACT

Surface expression of cell populations are often sought as diagnostic and prognostic biomarkers in hematology-oncology and infectious diseases, making flow cytometry an invaluable technique for both clinical and basic research applications. On the other hand, the reliance of flow cytometry on manual input parameters and user protocols for operation introduces variation between analyses while potentially leading to errors in measurements. In this work, we introduce an integrated flow cytometry microchip that automatically adapts to the sample it interrogates. Our device measures the antigen expression in a sample by automatically analyzing the response of immunomagnetically labeled cells to an external magnetic field through integrated electrical sensors and by continuously modulating the time the cells are subjected to the field for optimal sensitivity and dynamic range. Furthermore, the lack of optical illumination and fluorescence detectors enables automated analysis to be carried on a fully integrated platform that is particularly well suited for translation into point-of-care testing and mobile screening. We applied our automated cytometry chip on both pure and mixed cell populations and validated its operation by benchmarking against a conventional flow cytometer. By transforming the utility-proven flow cytometry, a technique that has long been dependent on an operator in centralized laboratories, into a standardized disposable test for bedside or home testing, the automated flow cytometry microchip introduced here has the potential to enable self-screening for telemedicine and wellness.

INTRODUCTION

Surface antigens, specialized proteins on the cell membrane, contain a treasure trove of information on a cell's identity, state, and function. They dynamically shift throughout the lifecycle of a cell and govern the cell's interaction with its external environment (Edelman and Crossin 1991; Gullberg et al. 2000), regulate various intracellular signaling pathways (Lemmon and Schlessinger 2010; Shipkova and Wieland 2012) as well as describe the lineage of the cell (Chen and Cherian 2017; Koay et al. 2016; Matarraz et al. 2017). From a clinical standpoint,

discrimination of the surface antigens is vital to diagnose oncological disorders (Gupta et al. 2018; Rawstron et al. 2018; Theunissen et al. 2017), hematological malignancies (Finak et al. 2016; Fouassier et al. 2020; Lacombe et al. 2016; Nickel et al. 2015) and infections (Estévez et al. 2020; Kennedy and Wilkinson 2017). They also are utilized to specifically target a cell type in therapies and therefore are widely studied for drug design (Haubner et al. 2019; Lee et al. 2018; Lv et al. 2018). As such, tools that can analyze expression of these important proteins on cell surface are crucial part of clinical and biotechnology research workflows.

The surface expression of a suspended cell population is universally analyzed by flow cytometry (Shapiro 2003). The cells are first tagged with fluorophores and then individually assessed under optical illumination and the surface expression is measured from the intensity of the resulting fluorescence emission. These analyses however are performed within a complex instrumental setup that relies on harmonious operation of various discrete optical, fluidic and electronic components, all of which drive costs of acquisition, operation and maintenance as well as leading to a substantial footprint (Cho et al. 2010). Consequently, the instrument is often deployed as a shared resource in centralized laboratories posing limited access for smaller peripheral clinics let alone for point-of-care (PoC) or mobile testing (Cho et al. 2010; Moore and Roederer 2009). Importantly, an extensive number of operational parameters need to be manually chosen together with the required sample preparation makes the whole process and the interpretation of results dependent on the specific operator/laboratory performed the analysis (Grant et al. 2021; Gratama et al. 2002; Pedersen et al. 2017).

To address the lack of flow cytometers amenable for mobile testing, low-cost, lab-on-a-chip (LoC) devices present an exciting alternative. LoC flow cytometers of various designs including those employing miniaturized laser systems (Murat et al. 2017; Skommer et al. 2013), viscoelastic fluids (Asghari et al. 2017), antibody microarrays (Liu et al. 2019; Liu et al. 2020), opto-fluidics (Göröcs et al. 2018; Zhu et al. 2011; Zhu and Ozcan 2015) as well as the ones that utilize electrical impedance (Du et al. 2013) and magnetic susceptibility (Civelekoglu et al. 2019b; Poudineh et al. 2017) measurements have been reported. While highly effective at addressing the instrumental complexity and bulkiness of conventional flow cytometers, these miniaturized cytometers still rely on manual user intervention to ensure optimal operational conditions and necessitate preliminary knowledge on the sample and its properties. Therefore, cell heterogeneity within a sample may easily cause saturation of the readout (Gaigalas and Wang 2008; Hoffman 2008), or various physical properties such as size and stiffness may hinder device operation (Dressaire and Sauret 2017) if not accounted for by the operator.

In this work, we developed an automated, microchip-based flow cytometry system that continuously adapts its operation to the specific sample under test for optimal analysis, and therefore, does not require external input from the user. Our device probes surface expression from the magnetic load carried by a cell labeled with antibody-conjugated magnetic beads. The entire process is performed within a microchip as no light sources and optical detectors are required for measurements. Instead, we (1) monitor trajectories magnetically manipulated cell via integrated electrical sensors, (2) compute surface expression of processed cell in real-time, (3) make decisions on the fitness of the instantaneous operational state through a deep-learning

computational model and (4) update the driving pressure via closed-loop feedback control to constantly optimize the field exposure on cells. When combined, these strategies resulted in a portable system that could automatically evaluate the expression level boundaries within a sample and then judiciously modulate the analysis conditions throughout the assay to maximize dynamic ratio from a minimal number of cells.

RESULTS

Assay workflow and physical design

Our assay relies on differential magnetophoretic responses among immunomagnetically labeled cells according to their surface expression and tracking those responses in real-time for measurements, decision-making, and feedback control of sample processing. A sample is first labeled against the target membrane antigen with 1 μm-diameter magnetic beads conjugated with antigen-specific antibodies. Labeled cells are then driven through our microchip, where they are subjected to a magnetic field gradient throughout the microfluidic channel (Figure 1a). This setup allows every cell to follow a distinct magnetophoretic trajectory, which depends on the flow rate (i.e., magnetic field exposure time), its size (i.e., resistance to transverse movement) and its magnetic load (i.e., surface expression of the target antigen) (Civelekoglu et al. 2019b; McCloskey et al. 2000; McCloskey et al. 2003). These trajectories are then transduced into electrical signals through a network of distributed Coulter sensors (Coulter 1956; Deblois and Bean 1970) placed at the end of the sorting stage, analyzed by a deep learning model in real-time to compute the expression of the surface marker of interest. For each cell, we concurrently compute a measurement score, which signifies the fitness of the operational parameters of the system for the estimated surface expression of level of the specific cell. Based on these measurement scores, we continuously adjust the sample driving pressure to modulate the exposure of cells to the magnetic field. This active closed-loop control on processing parameters allowed us to analyze samples without any preliminary knowledge such as the mean expression level or the expression range.

Our microchip is composed of fluidic, magnetic, and electrical components (Fig. 1b). The microfluidic channels hydrodynamically focus cells via sheath buffer flow. Magnetic deflection of the labeled cells occurs within a 1-cm by 3-mm chamber, which is positioned alongside a permanent magnet tasked with establishing a magnetic field gradient on the microchip. At the end of the deflection channel is the measurement stage, where fractionated cell population is distributed among eight discrete 30 μm-wide channels (Fig. 1c). These channels are monitored by an embedded code-multiplexed electrical sensor network (Liu et al. 2016), which is tasked with transducing on-chip trajectories and sizes of individual cells into electrical data. While there is a dedicated sensor for each channel, all are electrically connected for simultaneous reading over a single electrical output. To identify signals from a specific sensor in the network, sensors are micromachined on the channel floor to form distinct electrode patterns producing unique 15-bit code signals (Table 1) (Fig. 1d). For each sensor, specific arrangement of the positive and negative electrode fingers around a power trace encoded the intended digital code (Fig. 1d). Each electrode finger is designed to be 5 μm in width with 5 μm in between, creating a 305 μm-long sensor in each of the outlets. When a particle (i.e., cells) flow through one of these patterned

sensors, the sequential modulation in the channel impedance dictates an electrical signature waveform dictated by the underlying pattern (Fig. 1e).

Our device was fabricated on a glass substrate measuring 4-cm by 2-cm (Methods) (Fig. 1b). Briefly, the microfluidic layer was fabricated out of polydimethylsiloxane (PDMS) using soft lithography from a SU-8 patterned silicon wafer mold. The electrical sensors were surface micromachined out sensors out of 0.5 μm-thick film of gold and chromium. Specific electrode patterns were defined through photolithography and realized through a lift-off process. Microfluidic channels were formed by aligning and bonding the molded PDMS layer with the glass substrate after both surfaces were activated in oxygen plasma. As the final step, a permanent magnet was placed on the designed spot marked with photolithographically defined features to achieve the desired field gradient within the microfluidic channels repeatably.

Real-time processing of the device output signal

To process electrical signals from the device, we designed a data processing system that amplifies, digitizes, and analyzes incoming waveform in real-time. The hardware part of system was composed of a lock-in amplifier for extracting sensor signals with maximal signal-to-noise ratio and a data acquisition board for continuously sampling the data into a computer (Methods). The software part of the system was an algorithm written in Python for simultaneous data analysis. Our data processing system automatically extracted the cell events (sensor waveforms) from the idle section by periodically calculating the power of the incoming data block (50 samples a time). If a data block was identified as part of an active sensor event, corresponding data would be stored in a buffer, or else was discarded. These temporarily stored sensor waveforms were then forwarded to our deep learning model for interpretation.

To automatically recognize signature sensor waveforms in the data, we implemented our deep learning model based on the work by Wang et al. (Wang et al. 2019). The model is composed of two cascaded convolutional neural networks (ConvNet) (Fig. S1a), which are special deep learning structures commonly used in signal processing (Kiranyaz et al. 2021; Wang et al. 2019). This cascaded structure was previously shown to extract cell properties embedded in the electrical sensor waveforms with great accuracy, precision, and a high throughput over 700 cells per second (Wang et al. 2021; Wang et al. 2019). Briefly, the first ConvNet in the model, the region proposal network (RPN), identified the temporal location of each individual cell event by estimating a bounding box for each signature waveform identified. In this process, the network estimated both the power and the duration of each signature waveform, revealing the size and the velocity of corresponding cells. The second ConvNet of the cascade, the sensor classification network (SCN), then predicted the sensor identity (i.e., the trajectory of the corresponding cell) for each of signature waveform to which a bounding box was assigned by the RPN. While tasked with two different objectives, the RPN and SCN were structurally similar with each ConvNet containing four convolutional layers (Fig. S1b) with an input layer accepting the waveforms normalized to 200 samples. They differed in their output, as the, RPN produced 12 nodes, three of which were reserved for the number of coincident signature waveforms present in the signal block under test and the remaining nine were for the bounding box coordinates (i.e., the size and the speed of those cells). The output of the SCN, on the other hand, contained eight nodes, each

of which represented one of the eight sensors embedded in the device. Therefore, the combined output from our model was the sensor identity detecting the cell together with the time of detection, cell size and speed. The data augmentation, training, validation process we used to train our model along with the performance metrics of a similar model were described in detail by Wang et al. (Wang et al. 2019).

Linking on-chip cell behavior to surface antigen expression

To estimate the expression level of the target antigen from the magnetophoretic trajectory of a particular cell, we modeled forces acting on the immunomagnetically-labeled cell as it traverses our device. Because the on-chip trajectory of a cell depends on its size (i.e., drag forces), velocity (i.e., magnetic field exposure time) and surface antigen expression (i.e., magnetic force), we developed a finite element analysis model of our system that accounts for these forces of different origins (Methods). Using our model, we first swept the cell size, magnetic load, and flow speed over plausible ranges to determine the operational parameter space (Fig. 2a). From these simulations, we observed that the transverse deflection of the cell (i) increased with increased surface expression due to the larger magnetic force, (ii) decreased with increasing driving pressure due to shorter exposure time, and (iii) decreased with increasing cell size due to larger transverse drag force as anticipated.

Next, we extrapolated results from those simulated discrete cases to derive closed form analytic expressions for magnetic load on a cell given the specific electrical sensor detecting it. For each coded sensor, we first created a separate transfer function (Table 2) by fitting polynomial functions (Methods) of cell size and operating pressure to the finite element analysis (FEA)-simulated grids for calculating the maximum magnetic load a cell detected by that specific sensor can have (Fig. 2b). Because the 7^{th} sensor (i.e., the furthest one) does not have an upper limit for magnetic load, we instead derived a relation for the minimum magnetic load for cells to be sorted into that outlet. When inspected comparatively, these transfer functions showed that the estimated maximum magnetic load increased (1) with the receiving sensor being further (i.e., greater transverse deflection), (2) for larger cells as more magnetic load is needed to overcome greater size-induced drag, and (3) for higher pressure as greater magnetic force is needed to perform the same amount of work in a shorter time). We also tested the collective fitness of these transfer functions to the whole parameter space and ensured the derived relations approximate the simulated grid for different combinations of cell size, drive pressure and sensors (Fig. 2c). Taken together, constructing a closed-form transfer function instead of a discrete look-up table as in our previous work (Civelekoglu et al. 2017; Civelekoglu et al. 2019a, b; Civelekoglu et al. 2019c) facilitated faster computation for real-time analysis and reduced quantization errors leading to improved resolution in our calculations.

Finally, we calibrated electrical sensor signals to measure cell size and speed. To calibrate size measurements, we used commercially available polystyrene beads of 15 μm in diameter. These beads were chosen for calibration as they have a uniform size controlled by the manufacturer and also are similar in size to the cells employed in this study. Once the beads were processed by neural networks, we took the mean height of the resulting bounding boxes to represent a 15 μm cell (Fig. 2d). In this process, our calibration variable was proportional to the square of the cell

volume as (1) our measurement was based on the signal power and (2) the peak amplitude of the sensor signal is proportional to the cell size based on the Coulter principle (Deblois and Bean 1970). Likewise, we estimated cell flow speed from the duration of sensor code signals. Because the designed sensor length was known, the speed of a cell flowing by the sensor could be determined by dividing the sensor length to the signal duration. Testing these calculations at difference sample drive pressures, we found a linear relationship between the drive pressure and cell speed as anticipated (Fig. 2e). While we could digitally acquire the drive pressure information from the pressure regulator for this study, an independent an independent measurement of the pressure from calibrated cell flow speed measurements allows closed-loop control of operating conditions irrespective of the capabilities of the pressure source.

Adaptive control of the immunomagnetic cell manipulation

To automatically optimize magnetic field exposure for a given cell population, we first developed a feedback control scheme where the device adapts to the sample under interrogation by rapidly searching for the minimum exposure time needed for discriminating highest expressor cells (Fig. 3a). Specifically, we determine the saturation pressure which leads to all of the cells in the sample to be sorted exclusively into either one of the two closest sensors (i.e., sensor 0 or sensor 1). Because an increase in the flow rate beyond this point would lead to a saturated measurement that fails to differentiate cells based on their magnetic load, we operate our device below this saturation pressure for measurements. To search for the saturation pressure, we continuously analyzed the utilization of sensors by the sorted cells in real-time and aimed to minimize the error term (i.e., weighted utilization of the outer sensors that penalizes for cells received by further sensors) by electrically adjusting the drive pressure with a closed-loop control (Methods).

We tested the developed control scheme on magnetically labeled SK-BR-3 breast cancer cells and evaluated the system performance with different control parameters. Among tested conditions, we identified that a feedback gain of 1 and an update period of 20 cells led to minimal overshoot and the system reaching a steady state within a practically feasible number of cell measurements (Fig. S2). Under these settings, the terminal sensor utilization was found to be stable, with only the closest two sensors active as desired, after 35 iterations (~700 cells) in <2 minutes (Fig. 3b). The sample drive pressure was also observed to monotonically converge to the saturation pressure (~71 mbar) for the specific cell population used in this experiment (Fig. 3c) demonstrating a success search process.

Next, we attempted to optimize device operation for different expression levels. To quantitatively evaluate how well the instantaneous operational state of the system fits the sample under test, we first developed a scoring scheme for expression estimations (Fig. 3d). Because our system estimated cell magnetic load to be within a certain range due to sensor quantization (Fig. 3d (I)), we aimed to develop a scoring scheme that promoted less spread in these estimations for a given sample. For scoring purposes, we grouped measurements on cells with similar expression levels and assigned them to one of 20 bead-wide magnetic load windows based on the mean magnetic load (Fig. 3d (II)). Each magnetic load window was then assigned a measurement score calculated by dividing the number of analyzed cells in that magnetic window to the average

spread in the magnetic bead count estimations up to that point (Fig. 3d (III)). Using the transfer functions created for our sensors, we then determined the optimal drive pressure expected to maximize the measurement score for a magnetic load window (Fig. 3e) (Methods).

Combining these optimization processes, we designed an iterative process to automatically measure target membrane antigen expression in a cell population (Fig. 3f). During sample analysis, the system first searched for the saturation flow rate. Then, starting from the magnetic load window corresponding to the saturation flow rate, we adjusted the device state to apply pressure that was optimal for the magnetic load window. As cells were detected and analyzed in real time, we continuously calculated measurement score to evaluate the fitness of the measurements. Once the target score is reached, the algorithm moves the next magnetic load window and adjusts the device state to operate under the new optimal pressure. To ensure against premature termination, a minimum of 100 cell measurements was required at conditions optimized for each magnetic load, while a maximum limit clause of 200 cell measurements was imposed for any operational state in the algorithm to prevent the system to fall into a perpetual operation. This process iterated until the analysis can be performed optimally for each magnetic load window.

Analysis of homogeneous cell suspensions

While our technique can be applied to measurement surface expression of any target antigen irrespective of the cell type, we processed 3 different cancer cell lines, MDA-MB-231, LNCaP and MCF-7 cells, which are known to commonly express the epithelial cell adhesion molecule (EpCAM) at varying levels to test our measurement technique. The cell lines were cultured and split into two groups for this study: one group to be processed with magnetophoretic cytometry (i.e., test sample) and the other to be analyzed as control with fluorescence-based flow cytometry (i.e., control sample). Test samples were magnetically labeled with 1 μm magnetic beads conjugated with anti-EpCAM antibody (Methods), while the control samples were fluorescently labeled for flow cytometry (Methods).

To investigate the automated response of our system to different samples, we compared the evolution of the device state during the assays with the three cell lines. First, we observed that the saturation pressure that the feedback control system determined for MDA-MB-231, LNCaP and MCF-7 test samples were 59, 73 and 93 mbar, respectively (Fig. 4a). Because a higher saturation pressure for a sample signifies the field exposure needed to be lowered more for discrimination, these results indicated that MCF-7 cells would be the highest expressor, while MDA-MB-231 cells would be the lowest expressor for EpCAM among the three tested samples. Next, we examined the evolution of drive pressure and corresponding measurement scores as all expression levels are swept for each sample (Fig. 4b). We observed that the algorithm automatically adjusted the operational state with each iteration, and the target scores for magnetic load windows were reached for all tested samples.

Measurements on test samples showed that LNCaP cells were the smallest among the three with an average size of only 14.8 μm and had the minimum variation in size (STD = 4.48). MCF-7 and MDA-MB-231 cells, on the other hand, were similar in size with mean sizes of 20.1 μm

(STD =6.91) and 22.3 μm (STD 9.23), respectively (Fig. 4c). As for the EpCAM expression, the MDA-MB-231 cells had the lowest expression with an average magnetic load of 73 beads (median = 62, mode = 51, STD = 54.80), while LNCaP cells had 161 beads on average (median = 148, mode = 67, STD = 77.49) and MCF-7 cells carried an average of 225 beads (median = 203, mode = 197, STD = 113.22) (Fig. 4d). The ranking between the measured mean EpCAM expression level of these cell lines were indeed in agreement with the ranking of saturation pressure measured by our system. Finally, we repeated these measurements for each population (n=3) and proved repeatability of the assay (Fig. S3).

To validate our measurements, we independently analyzed matching control samples with a commercial fluorescence-based flow cytometer (Fig. 4e). In these measurements, we used the forward scatter width parameter (FSC-W), which depends linearly to the cell diameter (Shapiro 2003), to represent the size of the cells (Methods). Based on control sample data, MCF-7 cells were the largest with an average size of 20.93 μm (STD = 2.96) while MDA-MB-231 cells having a mean size of 19.48 μm (STD = 1.94) and LNCaP cells being the smallest among the three with a mean size of 16.79 μm (STD = 2.70). Comparing their surface expressions (Fig. 4f), MDA-MB-231 cells was the dimmest among the 3 cell lines under the same laser configuration. They exhibited a mean anti-EpCAM conjugated phycoerythrin (PE) intensity of 929 units, whereas LNCaP and MCF-7 populations had a mean intensity of 41,954 and 59,034 units, respectively, proving that our technique successfully captured the differential characteristics of these populations. On the other hand, the separation between the measured EpCAM expression distributions from different cell lines were observed to be less pronounced with magnetic beads, especially when results from MDA-MB-231 cells are compared with results from other cell lines. This is a result of the lower dynamic range of our measurements compared to fluorescence-based measurements as our dynamic range was ultimately limited by the number of magnetic beads that a cell could accommodate on its surface.

Analysis of heterogeneous cell suspensions

Following the analysis of samples consisting of single cell lines, we attempted to process heterogeneous cell populations. For this purpose, we mixed MDA-MB-231 and MCF-7 cells in a ratio unknown to the operator and performed blinded tests. Similar to our previous study, each sample was split into two aliquots, one to be processed by our system and one with a commercial flow cytometer for validation (Methods). To differentiate one cell type from another, we used the surface expression profiles acquired from homogenous samples and identified the gating level as the intersection point between different surface expression distributions. As such, the gate for a MDA-MB-231 + MCF-7 mixture was set 91 beads such that in our experiments cells carrying less than 91 magnetic beads were scored as MDA-MB-231 cells, while the rest were identified as MCF-7 cells.

Next, we investigated the automated analysis process while the cell mixture was processed with our system. A pressure sweep was initially performed by the system, which determined 140 mbar as the saturation pressure after analyzing 520 cells within 26 iterations (Fig. 5a). The surface expression was then analyzed by dynamically adjusting flow rate and the analysis was concluded

by reaching all score targets within 30 iterations (i.e., 30 different operational conditions for optimal measurements) (Fig. 5b).

From our analysis of the mixed sample, we observed a bimodal EpCAM expression distribution with one peak centered around ~18-μm diameter and 50 magnetic beads and another peak around 17 μm-diameter and 110 magnetic beads (Fig. 5c). Gating these populations by the previously identified magnetic load of 91 beads for an MDA-MB-231 versus MCF-7 discrimination, we found that the lower EpCAM expressing population had a mean size of 19.71 μm with a mean EpCAM expression of 49 magnetic beads, whereas the cells in the higher expressor subpopulation exhibited a mean size of 20.33 μm and an average of 217 magnetic beads. The measured size and expression parameters from these two populations closely agreed with those from previously performed individual measurements from pure MDA-MB-231 versus MCF-7 populations demonstrating a valid discrimination between two cell lines in a mixed sample. Furthermore, we found that 66.6% of the analyzed cells belonged to the EpCAM-high subpopulation while 33.4% were EpCAM-low group, leading to an estimated mix ratio of ~2:1 for MCF-7:MDA-MB-231 cells in the mixture (Fig. 5d).

Finally, the control sample analyzed by the commercial flow cytometer also resulted in a bimodal distribution of surface expression (Fig. 5e). The results demonstrated two distinct populations that could be gated at 10k unit-fluorescence. The metrics in the FSC-W analysis showed that these gated populations had a similar size characteristic with measurements from our system. The mean diameters of the EpCAM-low and EpCAM-high populations were found to be 19.35 μm and 20.11 μm, respectively. As for their prevalence, EpCAM-high and EpCAM-low groups represented the 67.9% and 32.1% of the sample, respectively (Fig. 5f). The estimated high-expressor to low-expressor ratio of ~2.1:1 validated the capability of our system in discriminating cell populations within a heterogenous sample.

DISCUSSION

Given the heterogeneity of biological samples, the capability to accommodate atypical specimens with no prior information is of critical importance for a bioanalytical technique if the results were to be relied on for decision making in the clinics. In this work, we demonstrated a flow cytometer that constantly evaluates the adequacy of its operational parameters for the sample being processed and automatically adapts to the sample for optimal measurements. We achieve this dynamic behavior through a closed-loop feedback control system. Feedback systems have been utilized in different setups involving lab-on-a-chip devices to control syringe pumps (Lake et al. 2017; Postiglione et al. 2018), pressure regulators (Wang et al. 2021), and power supplies (Armani et al. 2006; Lao et al. 2000; Shih et al. 2011) to control various process variables such as fluid flow rate (Lake et al. 2017), material content (Postiglione et al. 2018), cell velocity (Wang et al. 2021), physical forces (Armani et al. 2006; Shih et al. 2011) and temperature (Lao et al. 2000). Previously, we demonstrated a proof of principle control system where an integrated sensor network was employed to monitor cell speeds at different locations across a microfluidic chip to adjust the pressure controller to maintain a set flow speed even in the presence of external perturbation (Wang et al. 2021). In contrast, the presented feedback control system in this work monitors instantaneous state of spatial fractionation of a cell population within a microfluidic

device, algorithmically evaluates the fitness of fractionation via a scoring mechanism and sets the feedback control on the spatial separation response of the sample to the applied stimuli. As such, our system can automatically adapt to any sample, regardless of the type of the target cell population, to differentiate healthy or abnormal cells via a series of algorithmically decided actions and conclude the process with no prior knowledge on the sample and no external input from the operator.

Importantly our automated surface expression measurements can be performed on a portable and disposable microchip. Not having to rely on immunofluorescence for surface expression measurements eliminates otherwise required external optical components and sample alignment. We instead use a sensor network integrated on the chip for measurements and utilize machine learning algorithms, computational models to convert audio-like time waveform into biological data. Analysis of acquired time waveforms can be performed in real-time with less computational resources than that would be required for image/video processing and enables us to form a closed-loop control on device operation based on instantaneous sample response within the device. While we employed a digitally controlled pump to continuously optimized processing conditions in this paper, sample exposure can alternatively be adjusted by changing the magnetic field gradient through an on-chip electromagnet further relaxing the reliance on specialized external hardware for the measurements.

Taken together, our work combines micromachining, physical modeling, signal processing, algorithmic feedback control to create a chip-based flow cytometer as an alternative to fluorescence-based flow cytometers (Table S2). The autonomous operation offers the potential to eliminate user-to-user and lab-to-lab variations in running and/or interpretation of the results, which presents a common struggle in clinical cytometry (Grant et al. 2021; Maecker et al. 2010; Mizrahi et al. 2018). Moreover, the capability to adapt to different samples or operational settings augmenting a portable device facilitate POC use. The ability to perform flow cytometry outside of central laboratories will enable new preventative measures (Wergeland et al. 2011), health monitoring (Demaret et al. 2021; Monneret and Venet 2016; Talukder et al. 2017), emergency testing (Bourgoin et al. 2019; Hausmann et al. 2009) and rapid bedside evaluation of a disease (Bourgoin et al. 2020; Kestens and Mandy 2017; Zhang et al. 2020).

METHODS

Fabrication. To fabricate the mold for the microfluidic layer, 25 μm-thick SU-8 photoresist (SU-8 2025, MicroChem) was spun on a silicon wafer and exposed using a maskless aligner (MLA-1500, Heidelberg). Upon the development of the uncured resin, the wafer was treated with trichloro(octyl)silane in a desiccator for eight hours to promote effortless pealing. Then, a 10:1 mixture (by weight) of PDMS and its crosslinker (Sylgard 184 kit, Dow Corning) was poured on the mold, degassed, and cured at 65°C for at least 4 hours. The cured PDMS was then peeled off and cut into individual chips. To fabricate the electrical sensors, a 2-inch by 3-inch glass microscope slide (6101, Premiere) was coated with 1.5 μm-thick negative lift-off resist (NR9-1500PY, Futurrex) using a spin-coater. A 2-by-2 grid of the electrode patterns were transferred onto the photoresist using a maskless aligner (MLA-1500, Heidelberg). Once the photoresist was developed, the glass slides were treated under reactive ion etcher for

descumming, and a 500 nm-thick film of gold and chromium stack was deposited on the glass slide. The sacrificial layer was lifted-off in an acetone bath under mild sonication, leaving the patterned electrode on the glass substrate. Finally, the glass slide was sliced into 4 individual devices using a wafer saw. To form the final device, the PDMS layer and the glass substrate with the sensors were treated under oxygen plasma for one minute, carefully aligned under a microscope and bonded at 65°C on a hot plate. Using the alignment mark placed in the design of the microfluidic layer, the neodymium magnet (B848, K&J Magnetics) was placed on its designated location under a microscope and secured using a two-part fast curing epoxy.

Computational modeling. To model the operation and the unique characteristics of the device, we created the design of our cytometer chip in COMSOL Multiphysics. There were three additional physics used to represent different aspects of the device operation. First, the magnetic field generated by the permanent magnet was modeled using the "Magnetic Fields, No Current" interface. This interface calculated the magnetic field gradient in and around of the chip, which will later be used to compute the magnetic force on a cell. Then, for the fluid flow, we employed the "Laminar Flow" interface and introduced the fluid with a pressure source driving it through the microfluidic features. To track the behavior of a cell when it is under the magnetophoretic sorting, we used "Particle Tracing for Fluid Flow" interface. We parameterized the input pressure, surface expression and cell size within the modeling environment, and swept all conditions in a time-dependent study to reveal the unique behavior of any combinations of the parameters. The cumulative data was then separated by the final fluidic channel the cell was received and visualized the results using different surface plots representing each fluidic channel. To calculate an analytical relationship, we analyzed how the final sorting result varied with respect to the operational variables.

To extrapolate by fitting a surface function over the model-generated data points, we used the internal curve fitting toolbox of MATLAB. A polynomial expression of $f(d,p) = c_0 + c_1 d + c_2 p + c_3 dp + c_4 p^2$ was chosen the represent the surface function with least absolute residual (LAR) activated in the fitting process, as it consistently yielded the smallest root mean square error (RMSE). The goodness of fit metrics for the resulting curves are provided in Table S1.

Size and velocity calibration. In our system, the size of the cell was calculated using the amplitude of the electrical signal based on Coulter principle. To calculate the cell size robustly from our bipolar and digital signals, we first calculated the power of the signal, which was proportional to square of the amplitude. Then, we calculate the velocity of a cell by dividing the physical length of our sensors to the duration of the signal. To calibrate these values, we introduced polystyrene beads of 15 μm size (Cat #: 18328-5, Polysciences) from both the cell and the buffer inlets. Upon recording the events, we set the mean power of the resulting signals to represent the size of 15 μm. For the velocity calculations, we run these particles under different pressures values and calculated the velocity of the induvial cells. At least 15,000 events were analyzed in individual tests.

Determination of the optimal pressures for magnetic load windows. We utilized our modeling results in Table 2 and analyzed feasible scenarios. First, the drive pressure was discretized with increments of 1 mbar, and the cell size was discretized with increments of 1 μm.

We treated each feasible cell size and sensor combination as a potential cell measurement. Combining these potential measurements, we calculated the corresponding values of unique measurements "N" (Fig. S4) and the spread in each measurement "L" (Fig. S5) for each magnetic load window under various drive pressures. Finally, the measurement score (i.e., the quotient of N and L) was computed for each magnetic load window under various drive pressures (Fig. S6), from which we could determine the drive pressure that yielded the maximum measurement score in each window (Fig. 3d).

Construction of the feedback loop. The error value was defined as a weighted sum of the difference between the measured process variable and the setpoint. Specifically, we defined $D = [D_1, D_2, \ldots D_8]$ as the measured process variable representing the sensor distribution (normalized number of cells detected by each sensor) in each iteration, $T = [T_1, T_2, \ldots T_8]$ as the corresponding setpoint, and $W = [W_1, W_2, \ldots W_8]$ as the weight vector. Then, the error value was calculated as the inner product of $(D - T)$ and W. Throughout the work, target distribution was set to $T = [0.5, 0.5, 0, 0, 0, 0, 0, 0]$ to find the pressure where only the first two sensors were utilized (i.e., boundary pressure) and weights were set to $W = [0, 0, 2, 2, 4, 4, 8, 0]$, penalizing the outer sensors with increasing costs. It should be noted that we set $W_8 = 0$ to eliminate any potentially faulty contributions of cells that were stuck at the bottom of the sorting chamber at lower flow speeds and mobilized again as the flow speed increased. The calculated error term was than multiplied with a global gain constant, *K*, and sent to the pressure regulator for the next pressure value.

Cell culture. The cell lines used in this work were obtained from American Type Culture Collection (ATCC). Dulbecco's Modified Eagle Medium (DMEM) (10-013-CV, Corning) was used as the base culture media for the MDA-MB-231 and MCF-7 cells, Roswell Park Memorial Institute Medium (RPMI 1640) (10-040-CV, Corning) was used for LNCaP cells and McCoy's 5A Medium (10-050-CV, Corning) was used for the SK-BR-3 cells. All base media were supplemented with 10% fetal bovine serum (FBS) (35-010-CV, Corning) and 1% Penicillin/Streptomycin (30-002-CI, Corning) antibiotics. The cell lines were cultured at 37°C and 5% CO_2 in an incubator. Once they cells reached a confluency of 80% in the flask, they were collected and suspended in 1X PBS.

Sample preparation. The cell populations were first labeled with biotin conjugated antibody for the target surface marker at the amount of 150 fg antibody per cell. The mixture was incubated for 20 minutes and washed after centrifugation to eliminate the excess antibody in the suspension. Then, Dynabeads MyOne C1 beads was taken into a small vial at the ratio of 300 beads per cell and washed twice with 3% bovine serum albumin (BSA) solution. The beads were then pelleted with a magnet, resuspended in 1X PBS to its original volume, and introduced to the cell suspension. The mixture was incubated for 30 minutes before an experiment.

Experimental process. Before introducing the sample, the magnetophoretic cytometer was treated with a blocking buffer (SuperBlock T20, ThermoFisher) to prevent non-specific binding and accumulation of free magnetic beads in the microfluidic environment. Then, the sample and the buffer solution were loaded into their reservoirs (10 mL syringes with custom-made airtight caps) to be introduced into the device using a pressure source. To capture the electrical signals,

the sensor network was excited with a 1.5 V sine wave at 1 MHz through the input power pads, and the electrical currents through the positive and negative probes were measured. The current signal was first transduced into voltage signals by trans-impedance amplifiers which was then captured via a lock-in amplifier (HF2LI, Zurich Instruments). The output of the lock-in amplifier was sampled to a computer using a data acquisition board (PCIe-6361, National Instruments) for real-time analysis of the incoming data.

Flow cytometry validation. To verify the experimental results, the sample used in the experiment was also analyzed in a flow cytometer. The validation vial of the sample was fluorescently labeled with phycoerythrin (PE) conjugated EpCAM antibody (324206, BioLegend) following the manufacturer's labeling protocol. The labeled sample was then introduced to the flow cytometer (LSR-II, BD Biosciences) and the laser parameters were adjusted for optimal readout (FSC: 275V, SSC: 275V and PE: 250V). At least 10,000 events were recorded for each sample. The flow cytometry data was then analyzed using FlowJo (FlowJo, LLC) software. For the size information, polystyrene beads of 15 μm size (Cat #: 18328-5, Polysciences) were analyzed under the flow cytometer. The beads yielded a mean forward scatter intensity (FSC-W) of 90,811 units during the analysis of homogenous samples while the validation group for heterogeneous samples had a mean of 89,121 units. These values were used to calculate the cell size from FSC-W data.

CONCLUSION

We demonstrated a new flow cytometry chip with an automated operation using neural networks and real-time feedback control. The system automation ensured the operation under optimal condition regardless of the heterogeneity in the sample as our algorithm dynamically adapts to the sample and expands its dynamic as needed by modulating the drive pressure. This approach is similar to how a high dynamic range image is constructed in digital photography. By processing the sample under various flow rates controlled by the feedback loop, we achieve results with accuracy and precision using only eight physical sensors embedded in the device. Our low-cost, disposable, and automated cytometer showed a promising utility in POC testing for health monitoring, emergency testing and bedside patient evaluation.

AUTHOR CONTRIBUTIONS

O.C., N.W. and A.F.S. designed the research and wrote the manuscript. O.C. designed the microfluidic components. N.W. designed the sensor structure. A.K.M.A and M.B. microfabricated the chip. N.W. designed the neural network for signal analysis. O.C. performed the flow cytometry analyses. O.C. and N.W. conducted the experiments. O.C., N.W. and A.F.S. analyzed the results. All authors have read and approved the manuscript.

ACKNOWLEDGEMENTS

The work was supported by the National Science Foundations (NSF) Awards No. ECCS 1610995 and ECCS 1752170, and the Arnold and Mabel Beckman Foundation (Beckman Young Investigator Award to A.F.S.).

REFERENCES

Armani, M.D., Chaudhary, S.V., Probst, R., Shapiro, B., 2006. Using feedback control of microflows to independently steer multiple particles. J Microelectromech S 15(4), 945-956.

Asghari, M., Serhatlioglu, M., Ortaç, B., Solmaz, M.E., Elbuken, C., 2017. Sheathless Microflow Cytometry Using Viscoelastic Fluids. Scientific Reports 7(1), 12342.

Bourgoin, P., Soliveres, T., Ahriz, D., Arnoux, I., Meisel, C., Unterwalder, N., Morange, P.E., Michelet, P., Malergue, F., Markarian, T., 2019. Clinical research assessment by flow cytometry of biomarkers for infectious stratification in an Emergency Department. Biomark Med 13(16), 1373-1386.

Bourgoin, P., Taspinar, R., Gossez, M., Venet, F., Delwarde, B., Rimmele, T., Morange, P.E., Malergue, F., Monneret, G., 2020. Toward Monocyte HLA-DR Bedside Monitoring: A Proof of Concept Study. Shock.

Chen, X., Cherian, S., 2017. Acute Myeloid Leukemia Immunophenotyping by Flow Cytometric Analysis. Clin Lab Med 37(4), 753-769.

Cho, S.H., Godin, J.M., Chen, C.-H., Qiao, W., Lee, H., Lo, Y.-H., 2010. Review Article: Recent advancements in optofluidic flow cytometer. Biomicrofluidics 4(4), 043001.

Civelekoglu, O., Liu, R.X., Boya, M., Chu, C.H., Wang, N.Q., Sarioglu, A.F., 2017. A Microfluidic Device for Electronic Cell Surface Expression Profiling Using Magnetophoresis. 2017 19th International Conference on Solid-State Sensors, Actuators and Microsystems (Transducers), 480-483.

Civelekoglu, O., Wang, N., Boya, M., Ozkaya-Ahmadov, T., Liu, R., Sarioglu, A.F., 2019a. Digital photography techniques in microfluidics: Exposure bracketing for high dynamic range magnetophoretic cytometry. Proc. 23rd International Conference on Miniaturized Systems for Chemistry and Life Sciences.

Civelekoglu, O., Wang, N., Boya, M., Ozkaya-Ahmadov, T., Liu, R., Sarioglu, A.F., 2019b. Electronic profiling of membrane antigen expression via immunomagnetic cell manipulation. Lab Chip 19(14), 2444-2455.

Civelekoglu, O., Wang, N.Q., Boya, M., Ozkaya-Ahmadov, T., Liu, R.X., Sarioglu, A.F., 2019c. Quantitative Measurement of Cell Surface Expression Via Magnetophoretic Cytometry. 2019 20th International Conference on Solid-State Sensors, Actuators and Microsystems & Eurosensors Xxxiii (Transducers & Eurosensors Xxxiii), 975-978.

Coulter, W.H., 1956. High speed automatic blood cell counter and cell size analyzer. Proceedings of the National Electronics Conference 12, 1034.

Deblois, R.W., Bean, C.P., 1970. Counting and Sizing of Submicron Particles by Resistive Pulse Technique. Rev Sci Instrum 41(7), 909-&.

Demaret, J., Varlet, P., Trauet, J., Beauvais, D., Grossemy, A., Hégo, F., Yakoub-Agha, I., Labalette, M., 2021. Monitoring CAR T-cells using flow cytometry. Cytometry Part B: Clinical Cytometry 100(2), 218-224.

Dressaire, E., Sauret, A., 2017. Clogging of microfluidic systems. Soft Matter 13(1), 37-48.

Du, E., Ha, S., Diez-Silva, M., Dao, M., Suresh, S., Chandrakasan, A.P., 2013. Electric impedance microflow cytometry for characterization of cell disease states. Lab Chip 13(19), 3903-3909.

Edelman, G.M., Crossin, K.L., 1991. Cell adhesion molecules: implications for a molecular histology. Annu Rev Biochem 60, 155-190.

Estévez, O., Anibarro, L., Garet, E., Martínez, A., Pena, A., Barcia, L., Peleteiro, M., González-Fernández, Á., 2020. Multi-parameter flow cytometry immunophenotyping distinguishes different stages of tuberculosis infection. Journal of Infection 81(1), 57-71.

Finak, G., Langweiler, M., Jaimes, M., Malek, M., Taghiyar, J., Korin, Y., Raddassi, K., Devine, L., Obermoser, G., Pekalski, M.L., Pontikos, N., Diaz, A., Heck, S., Villanova, F., Terrazzini, N., Kern, F., Qian, Y., Stanton, R., Wang, K., Brandes, A., Ramey, J., Aghaeepour, N., Mosmann, T., Scheuermann, R.H., Reed, E., Palucka, K., Pascual, V., Blomberg, B.B., Nestle, F., Nussenblatt, R.B., Brinkman, R.R., Gottardo, R., Maecker, H., McCoy, J.P., 2016. Standardizing Flow Cytometry Immunophenotyping Analysis from the Human ImmunoPhenotyping Consortium. Scientific Reports 6(1), 20686.

Fouassier, M., Babuty, A., Debord, C., Béné, M.C., 2020. Platelet immunophenotyping in health and inherited bleeding disorders, a review and practical hints. Cytometry Part B: Clinical Cytometry 98(6), 464-475.

Gaigalas, A.K., Wang, L., 2008. Approaches to Quantitation in Flow Cytometry. In: Resch-Genger, U. (Ed.), Standardization and Quality Assurance in Fluorescence Measurements II: Bioanalytical and Biomedical Applications, pp. 371-398. Springer Berlin Heidelberg, Berlin, Heidelberg.

Grant, R., Coopman, K., Medcalf, N., Silva-Gomes, S., Campbell, J.J., Kara, B., Braybrook, J., Petzing, J., 2021. Quantifying Operator Subjectivity within Flow Cytometry Data Analysis as a Source of Measurement Uncertainty and the Impact of Experience on Results. PDA Journal of Pharmaceutical Science and Technology 75(1), 33-47.

Gratama, J.W., Kraan, J., Keeney, M., Granger, V., Barnett, D., 2002. Reduction of variation in T-cell subset enumeration among 55 laboratories using single-platform, three or four-color flow cytometry based on CD45 and SSC-based gating of lymphocytes. Cytometry 50(2), 92-101.

Gullberg, E., Leonard, M., Karlsson, J., Hopkins, A.M., Brayden, D., Baird, A.W., Artursson, P., 2000. Expression of specific markers and particle transport in a new human intestinal M-cell model. Biochem Biophys Res Commun 279(3), 808-813.

Gupta, S., Devidas, M., Loh, M.L., Raetz, E.A., Chen, S., Wang, C., Brown, P., Carroll, A.J., Heerema, N.A., Gastier-Foster, J.M., Dunsmore, K.P., Larsen, E.C., Maloney, K.W., Mattano, L.A., Winter, S.S., Winick, N.J., Carroll, W.L., Hunger, S.P., Borowitz, M.J., Wood, B.L., 2018. Flow-cytometric vs. -morphologic assessment of remission in childhood acute lymphoblastic leukemia: a report from the Children's Oncology Group (COG). Leukemia 32(6), 1370-1379.

Göröcs, Z., Tamamitsu, M., Bianco, V., Wolf, P., Roy, S., Shindo, K., Yanny, K., Wu, Y., Koydemir, H.C., Rivenson, Y., Ozcan, A., 2018. A deep learning-enabled portable imaging flow cytometer for cost-effective, high-throughput, and label-free analysis of natural water samples. Light: Science & Applications 7(1), 66.

Haubner, S., Perna, F., Köhnke, T., Schmidt, C., Berman, S., Augsberger, C., Schnorfeil, F.M., Krupka, C., Lichtenegger, F.S., Liu, X., Kerbs, P., Schneider, S., Metzeler, K.H., Spiekermann, K., Hiddemann, W., Greif, P.A., Herold, T., Sadelain, M., Subklewe, M., 2019. Coexpression profile of leukemic stem cell markers for combinatorial targeted therapy in AML. Leukemia 33(1), 64-74.

Hausmann, O.V., Gentinetta, T., Bridts, C.H., Ebo, D.G., 2009. The Basophil Activation Test in Immediate-Type Drug Allergy. Immunology and Allergy Clinics of North America 29(3), 555-566.

Hoffman, R.A., 2008. Flow Cytometry: Instrumentation, Applications, Future Trends and Limitations. In: Resch-Genger, U. (Ed.), Standardization and Quality Assurance in Fluorescence Measurements II: Bioanalytical and Biomedical Applications, pp. 307-342. Springer Berlin Heidelberg, Berlin, Heidelberg.

Kennedy, D., Wilkinson, M.G., 2017. Application of Flow Cytometry to the Detection of Pathogenic Bacteria. Curr Issues Mol Biol 23, 21-38.

Kestens, L., Mandy, F., 2017. Thirty-five years of CD4 T-cell counting in HIV infection: From flow cytometry in the lab to point-of-care testing in the field. Cytometry Part B: Clinical Cytometry 92(6), 437-444.

Kiranyaz, S., Avci, O., Abdeljaber, O., Ince, T., Gabbouj, M., Inman, D.J., 2021. 1D convolutional neural networks and applications: A survey. Mechanical Systems and Signal Processing 151, 107398.

Koay, H.-F., Gherardin, N.A., Enders, A., Loh, L., Mackay, L.K., Almeida, C.F., Russ, B.E., Nold-Petry, C.A., Nold, M.F., Bedoui, S., Chen, Z., Corbett, A.J., Eckle, S.B.G., Meehan, B., d'Udekem, Y., Konstantinov, I.E., Lappas, M., Liu, L., Goodnow, C.C., Fairlie, D.P., Rossjohn, J., Chong, M.M., Kedzierska, K., Berzins, S.P., Belz, G.T., McCluskey, J., Uldrich, A.P., Godfrey, D.I., Pellicci, D.G., 2016. A three-stage intrathymic development pathway for the mucosal-associated invariant T cell lineage. Nature Immunology 17(11), 1300-1311.

Lacombe, F., Bernal, E., Bloxham, D., Couzens, S., Porta, M.G.D., Johansson, U., Kern, W., Macey, M., Matthes, T., Morilla, R., Paiva, A., Palacio, C., Preijers, F., Ratei, R., Siitonen, S., Allou, K., Porwit, A., Béné, M.C., 2016. Harmonemia: a universal strategy for flow cytometry immunophenotyping—A European LeukemiaNet WP10 study. Leukemia 30(8), 1769-1772.

Lake, J.R., Heyde, K.C., Ruder, W.C., 2017. Low-cost feedback-controlled syringe pressure pumps for microfluidics applications. Plos One 12(4).

Lao, A.I.K., Lee, T.M.H., Hsing, I.M., Ip, N.Y., 2000. Precise temperature control of microfluidic chamber for gas and liquid phase reactions. Sensors and Actuators A: Physical 84(1), 11-17.

Lee, Y.T., Tan, Y.J., Oon, C.E., 2018. Molecular targeted therapy: Treating cancer with specificity. European Journal of Pharmacology 834, 188-196.

Lemmon, M.A., Schlessinger, J., 2010. Cell Signaling by Receptor Tyrosine Kinases. Cell 141(7), 1117-1134.

Liu, R., Chu, C.H., Wang, N., Ozkaya-Ahmadov, T., Civelekoglu, O., Lee, D., Arifuzzman, A.K.M., Sarioglu, A.F., 2019. Combinatorial Immunophenotyping of Cell Populations with an Electronic Antibody Microarray. Small 15(51), e1904732.

Liu, R., Wang, N., Kamili, F., Sarioglu, A.F., 2016. Microfluidic CODES: a scalable multiplexed electronic sensor for orthogonal detection of particles in microfluidic channels. Lab Chip 16(8), 1350-1357.

Liu, R.X., Arifuzzman, A.K.M., Wang, N.Q., Civelekoglu, O., Sarioglu, A.F., 2020. Electronic Immunoaffinity Assay for Differential Leukocyte Counts. J Microelectromech S 29(5), 942-947.

Lv, Q., Yang, J., Zhang, R., Yang, Z., Yang, Z., Wang, Y., Xu, Y., He, Z., 2018. Prostate-Specific Membrane Antigen Targeted Therapy of Prostate Cancer Using a DUPA–Paclitaxel Conjugate. Molecular Pharmaceutics 15(5), 1842-1852.

Maecker, H.T., McCoy, J.P., Amos, M., Elliott, J., Gaigalas, A., Wang, L., Aranda, R., Banchereau, J., Boshoff, C., Braun, J., Korin, Y., Reed, E., Cho, J., Hafler, D., Davis, M., Fathman, C.G., Robinson, W., Denny, T., Weinhold, K., Desai, B., Diamond, B., Gregersen, P., Di Meglio, P., Nestle, F.O., Peakman, M., Villanova, F., Ferbas, J., Field, E., Kantor, A., Kawabata, T., Komocsar, W., Lotze, M., Nepom, J., Ochs, H., O'Lone, R., Phippard, D., Plevy, S., Rich, S., Roederer, M., Rotrosen, D., Yeh, J.-H., the, F.H.I.C., 2010. A model for harmonizing flow cytometry in clinical trials. Nature Immunology 11(11), 975-978.

Matarraz, S., Almeida, J., Flores-Montero, J., Lécrevisse, Q., Guerri, V., López, A., Bárrena, S., Van Der Velden, V.H.J., Te Marvelde, J.G., Van Dongen, J.J.M., Orfao, A., 2017. Introduction to the diagnosis and classification of monocytic-lineage leukemias by flow cytometry. Cytometry Part B: Clinical Cytometry 92(3), 218-227.

McCloskey, K.E., Chalmers, J.J., Zborowski, M., 2000. Magnetophoretic mobilities correlate to antibody binding capacities. Cytometry 40(4), 307-315.

McCloskey, K.E., Moore, L.R., Hoyos, M., Rodriguez, A., Chalmers, J.J., Zborowski, M., 2003. Magnetophoretic cell sorting is a function of antibody binding capacity. Biotechnol Prog 19(3), 899-907.

Mizrahi, O., Ish Shalom, E., Baniyash, M., Klieger, Y., 2018. Quantitative Flow Cytometry: Concerns and Recommendations in Clinic and Research. Cytometry Part B: Clinical Cytometry 94(2), 211-218.

Monneret, G., Venet, F., 2016. Sepsis-induced immune alterations monitoring by flow cytometry as a promising tool for individualized therapy. Cytometry Part B: Clinical Cytometry 90(4), 376-386.

Moore, J., Roederer, M., 2009. The Flow Cytometry Shared Resource Laboratory: Best practices to assure a high-quality, cost-effective partnership with biomedical research laboratories. Cytometry Part A 75A(8), 643-649.

Murat, S., Caglar, E., Bulend, O., Mehmet, E.S., 2017. Femtosecond laser fabrication of fiber based optofluidic platform for flow cytometry applications. Proc.SPIE.

Nickel, R.S., Horan, J.T., Fasano, R.M., Meyer, E., Josephson, C.D., Winkler, A.M., Yee, M.E.M., Kean, L.S., Hendrickson, J.E., 2015. Immunophenotypic parameters and RBC alloimmunization in children with sickle cell disease on chronic transfusion. American Journal of Hematology 90(12), 1135-1141.

Pedersen, N.W., Chandran, P.A., Qian, Y., Rebhahn, J., Petersen, N.V., Hoff, M.D., White, S., Lee, A.J., Stanton, R., Halgreen, C., Jakobsen, K., Mosmann, T., Gouttefangeas, C., Chan, C., Scheuermann, R.H., Hadrup, S.R., 2017. Automated Analysis of Flow Cytometry Data to Reduce Inter-Lab Variation in the Detection of Major Histocompatibility Complex Multimer-Binding T Cells. Frontiers in Immunology 8(858).

Postiglione, L., Napolitano, S., Pedone, E., Rocca, D.L., Aulicino, F., Santorelli, M., Tumaini, B., Marucci, L., di Bernardo, D., 2018. Regulation of Gene Expression and Signaling Pathway Activity in Mammalian Cells by Automated Microfluidics Feedback Control. ACS Synth Biol 7(11), 2558-2565.

Poudineh, M., Aldridge, P.M., Ahmed, S., Green, B.J., Kermanshah, L., Nguyen, V., Tu, C., Mohamadi, R.M., Nam, R.K., Hansen, A., Sridhar, S.S., Finelli, A., Fleshner, N.E., Joshua, A.M., Sargent, E.H., Kelley, S.O., 2017. Tracking the dynamics of circulating tumour cell phenotypes using nanoparticle-mediated magnetic ranking. Nature Nanotechnology 12(3), 274-281.

Rawstron, A.C., Kreuzer, K.-A., Soosapilla, A., Spacek, M., Stehlikova, O., Gambell, P., McIver-Brown, N., Villamor, N., Psarra, K., Arroz, M., Milani, R., de la Serna, J., Cedena, M.T., Jaksic, O., Nomdedeu, J., Moreno, C., Rigolin, G.M., Cuneo, A., Johansen, P., Johnsen, H.E., Rosenquist, R., Niemann, C.U., Kern, W., Westerman, D., Trneny, M., Mulligan, S., Doubek, M., Pospisilova, S., Hillmen, P., Oscier, D., Hallek, M., Ghia, P., Montserrat, E., 2018. Reproducible diagnosis of chronic lymphocytic leukemia by flow cytometry: An European Research Initiative on CLL (ERIC) & European Society for Clinical Cell Analysis (ESCCA) Harmonisation project. Cytometry Part B: Clinical Cytometry 94(1), 121-128.

Shapiro, H.M., 2003. Practical flow cytometry, 4th ed. Wiley-Liss, New York.

Shih, S.C., Fobel, R., Kumar, P., Wheeler, A.R., 2011. A feedback control system for high-fidelity digital microfluidics. Lab Chip 11(3), 535-540.

Shipkova, M., Wieland, E., 2012. Surface markers of lymphocyte activation and markers of cell proliferation. Clin Chim Acta 413(17-18), 1338-1349.

Skommer, J., Akagi, J., Takeda, K., Fujimura, Y., Khoshmanesh, K., Wlodkowic, D., 2013. Multiparameter Lab-on-a-Chip flow cytometry of the cellcycle. Biosensors and Bioelectronics 42, 586-591.

Talukder, N., Furniturewalla, A., Le, T., Chan, M., Hirday, S., Cao, X., Xie, P., Lin, Z., Gholizadeh, A., Orbine, S., Javanmard, M., 2017. A portable battery powered microfluidic impedance cytometer with smartphone readout: towards personal health monitoring. Biomed Microdevices 19(2), 36.

Theunissen, P., Mejstrikova, E., Sedek, L., van der Sluijs-Gelling, A.J., Gaipa, G., Bartels, M., Sobral da Costa, E., Kotrová, M., Novakova, M., Sonneveld, E., Buracchi, C., Bonaccorso, P., Oliveira, E., te Marvelde, J.G., Szczepanski, T., Lhermitte, L., Hrusak, O., Lecrevisse, Q., Grigore, G.E., Froňková, E., Trka, J., Brüggemann, M., Orfao, A., van Dongen, J.J.M., van der Velden, V.H.J., on behalf of the EuroFlow, C., 2017. Standardized flow cytometry for highly sensitive MRD measurements in B-cell acute lymphoblastic leukemia. Blood 129(3), 347-357.

Wang, N.Q., Liu, R.X., Asmare, N., Chu, C.H., Civelekoglu, O., Sarioglu, A.F., 2021. Closed-loop feedback control of microfluidic cell manipulation via deep-learning integrated sensor networks dagger. Lab Chip.

Wang, N.Q., Liu, R.X., Asmare, N., Chu, C.H., Sarioglu, A.F., 2019. Processing code-multiplexed Coulter signals via deep convolutional neural networks. Lab Chip 19(19), 3292-3304.

Wergeland, I., Aßmus, J., Dyrhol-Riise, A.M., 2011. T Regulatory Cells and Immune Activation in Mycobacterium tuberculosis Infection and the Effect of Preventive Therapy. Scandinavian Journal of Immunology 73(3), 234-242.

Zhang, S., Li, Z., Wei, Q., 2020. Smartphone-based cytometric biosensors for point-of-care cellular diagnostics. Nanotechnology and Precision Engineering 3(1), 32-42.

Zhu, H., Mavandadi, S., Coskun, A.F., Yaglidere, O., Ozcan, A., 2011. Optofluidic Fluorescent Imaging Cytometry on a Cell Phone. Anal Chem 83(17), 6641-6647.

Zhu, H., Ozcan, A., 2015. Opto-Fluidics Based Microscopy and Flow Cytometry on a Cell Phone for Blood Analysis. In: Rasooly, A., Herold, K.E. (Eds.), Mobile Health Technologies: Methods and Protocols, pp. 171-190. Springer New York, New York, NY.

Table 1. Spreading sequences used for multiplexing the sensors distributed throughout the magnetophoretic cytometer. The codes consist of 15 bits that were randomly generated with equal probabilities for being a "1" or a "0".

	Spreading sequence														
Sensor 0	0	1	0	0	1	1	0	1	1	0	0	1	0	0	0
Sensor 1	1	1	1	0	1	1	0	0	0	1	1	0	0	1	1
Sensor 2	1	0	1	0	0	1	1	1	0	0	1	0	1	0	1
Sensor 3	0	0	1	1	1	0	1	1	0	0	0	1	1	0	1
Sensor 4	1	0	1	1	0	0	0	1	0	1	1	0	1	1	0
Sensor 5	0	0	1	0	0	0	1	1	0	1	0	1	0	1	0
Sensor 6	1	0	1	1	0	1	1	0	0	1	0	1	0	0	1
Sensor 7	1	0	0	1	1	1	0	0	1	0	1	0	0	1	0

Table 2. Transfer functions for each sensor linking the cell behavior to the surface expression. The function f yields the maximum allowed magnetic load per sensor, and the input d denotes the diameter of a cell in µm, and the input p denotes the operating pressure in mbar.

Polynomial expression:	$f(d,p) = c_0 + c_1 d + c_2 p + c_3 dp + c_4 p^2$				
	c_0	c_1	c_2	c_3	c_4
Sensor 0	-2.557	0.5556	0.1156	0.03889	-0.000889
Sensor 1	-9.842	1.1213	0.6772	0.09074	-0.008407
Sensor 2	-12.78	1.593	1.159	0.1481	-0.01408
Sensor 3	-8.414	1.652	1.36	0.203	-0.01552
Sensor 4	-6.743	1.799	1.742	0.244	-0.01854
Sensor 5	-15.94	2.444	2.588	0.2511	-0.02379
Sensor 6	-12.59	2.693	2.494	0.2661	-0.02003
Sensor 7 (min. requirement)	-11.59	2.693	2.494	0.2661	-0.02003

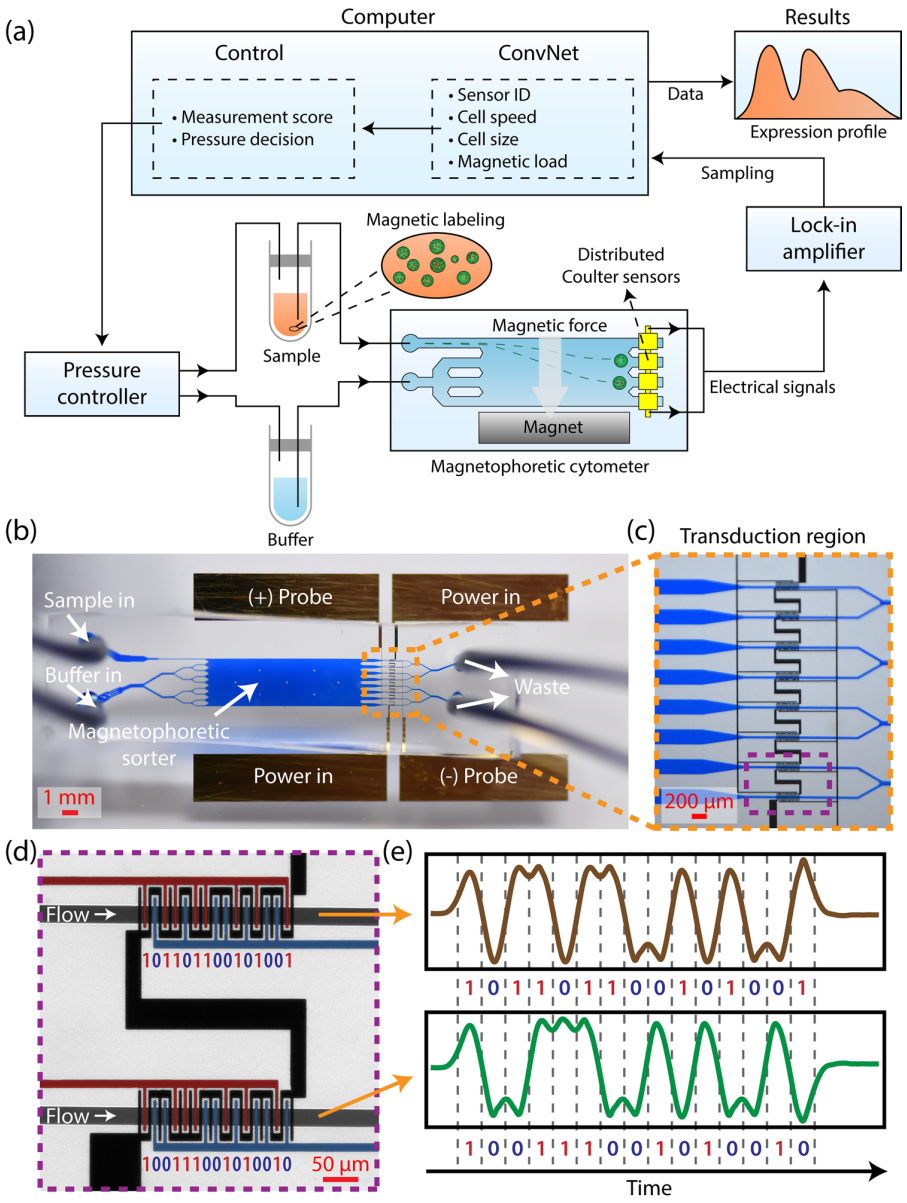

Fig. 1. Assay workflow and physical design. (a) Operation principle of the automated cytometer. The sample and buffer were driven into the magnetophoretic cytometer using a pressure controller. Convolutional neural networks processed the incoming data from the cytometer in real-time and forwarded the processed data to the controller for decision making. (b) A photo of the magnetophoretic cytometer chip. The fluidic channels were filled with color dye to represent their structure. (c) Close-up image of the sensing area where the cell information is transduced into unique electrical signals. (d) Digital code-multiplexing of the electrical sensors. (e) Electrical signals corresponding to the Sensor 6 and Sensor 7.

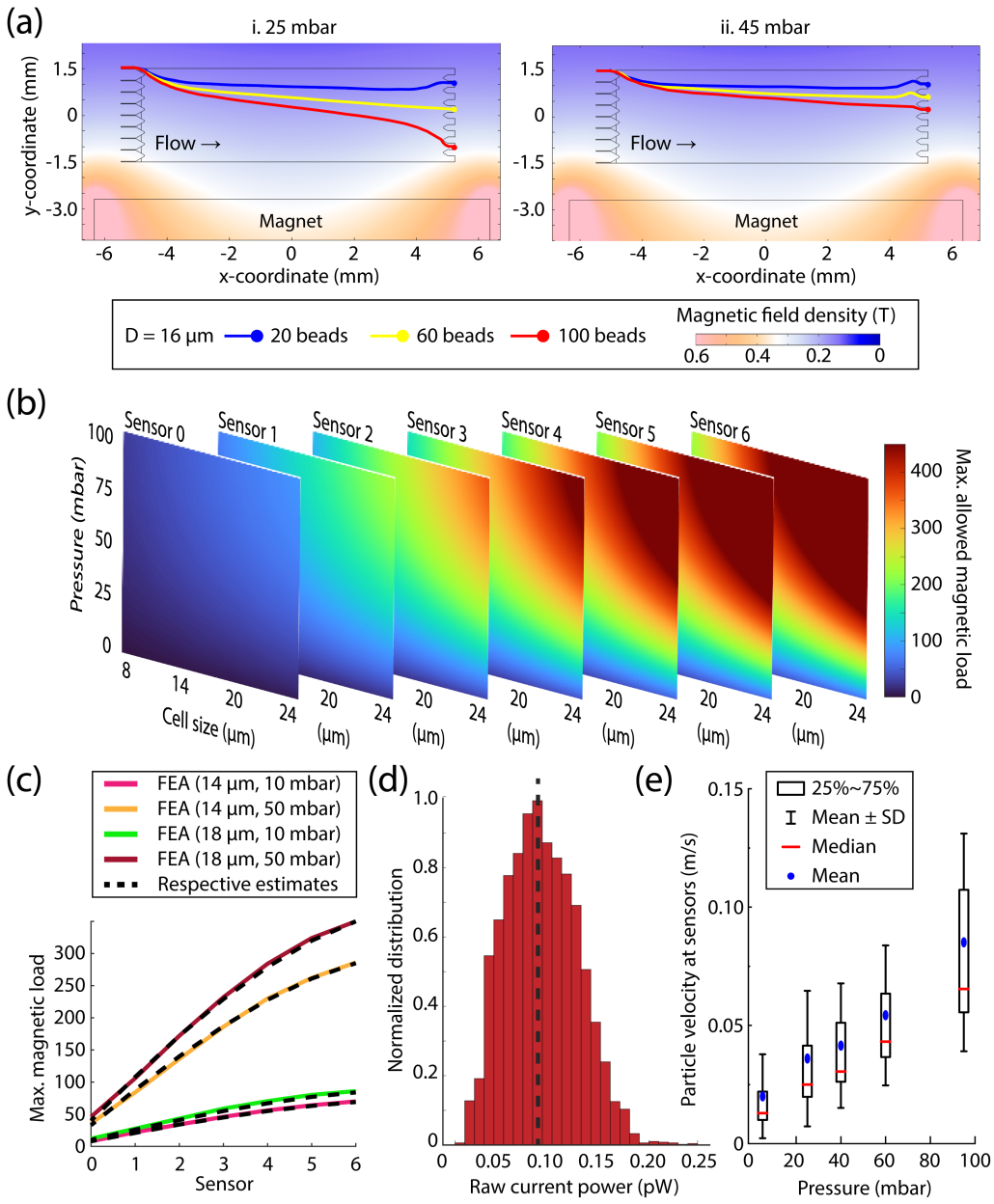

Fig. 2. Computational modeling and the characterization of the cytometer. (a) Finite element analysis of the magnetophoretic sorting based on device properties. Changing the flow rate creates different sorting dynamics that allows us to achieve a higher dynamic range. (b) Multidimensional mapping of between the cell size, pressure, magnetic load and the sensors. (c) Comparison between raw data and the analytical representation of the mapping. (d) The calibration of cell size from the signal power using 15 µm beads. (e) Analysis of the particle velocity with respect to the drive pressure.

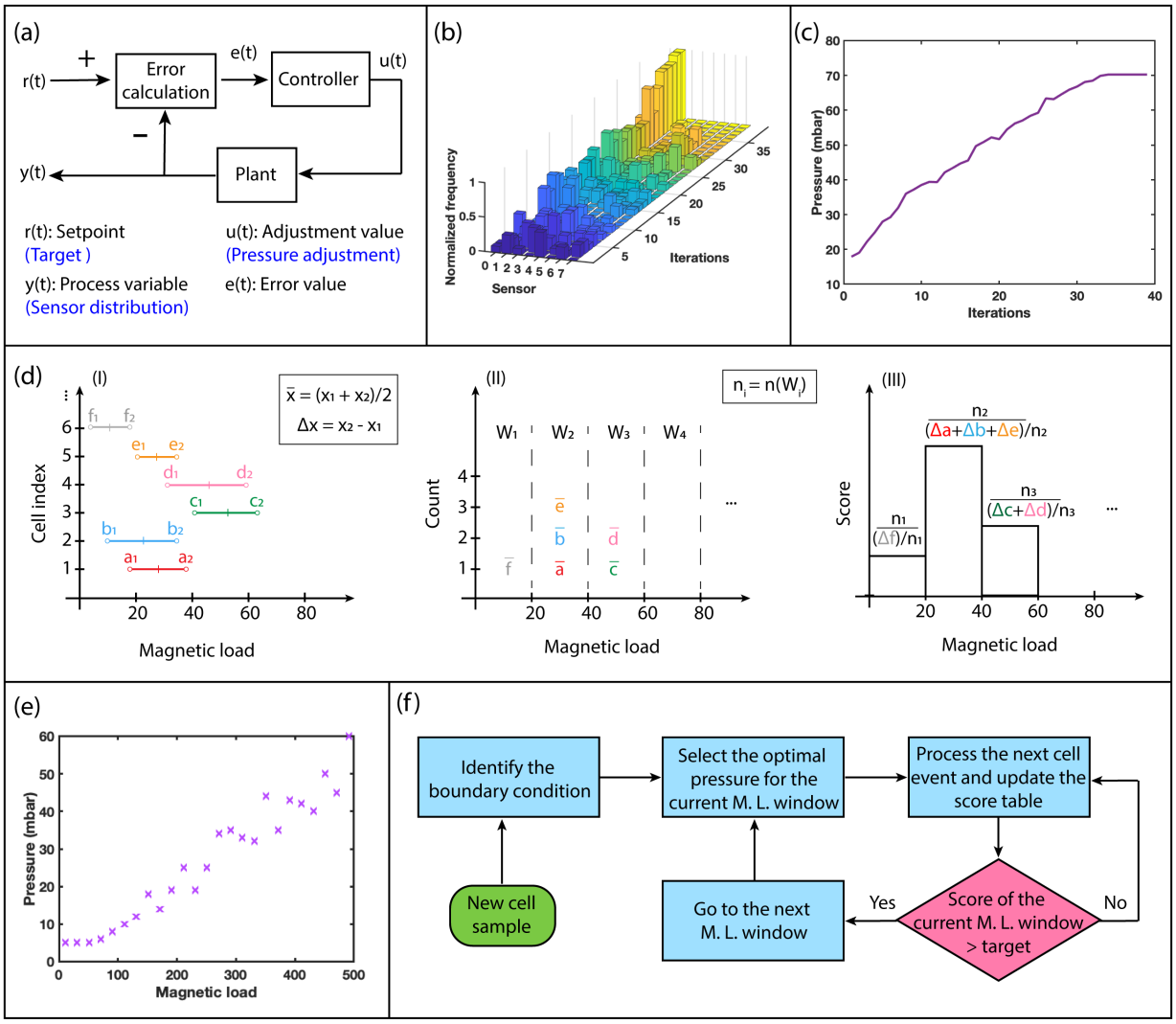

Fig. 3. Automating of Surface Expression Measurements. (a) The feedback mechanism used to determine the boundary pressure. (b) Time evolution of the sensor distribution when determining the boundary pressure. (c) Time evolution of the drive pressure when determining the boundary pressure. (d) Defining of measurement score. Each cell with a specific magnetic load range is mapped to a magnetic load window based on the mean of the range (denoted as $\bar{x}$). For each magnetic load window (denoted as W_i), the measurement score is defined as the quotient of the number of distinct cells in a window (denoted as n_i) and the average length of magnetic load ranges in that window (each range is denoted as Δx). (e) The optimal pressure of each magnetic load window. (f) The workflow for optimizing the surface expression measurement.

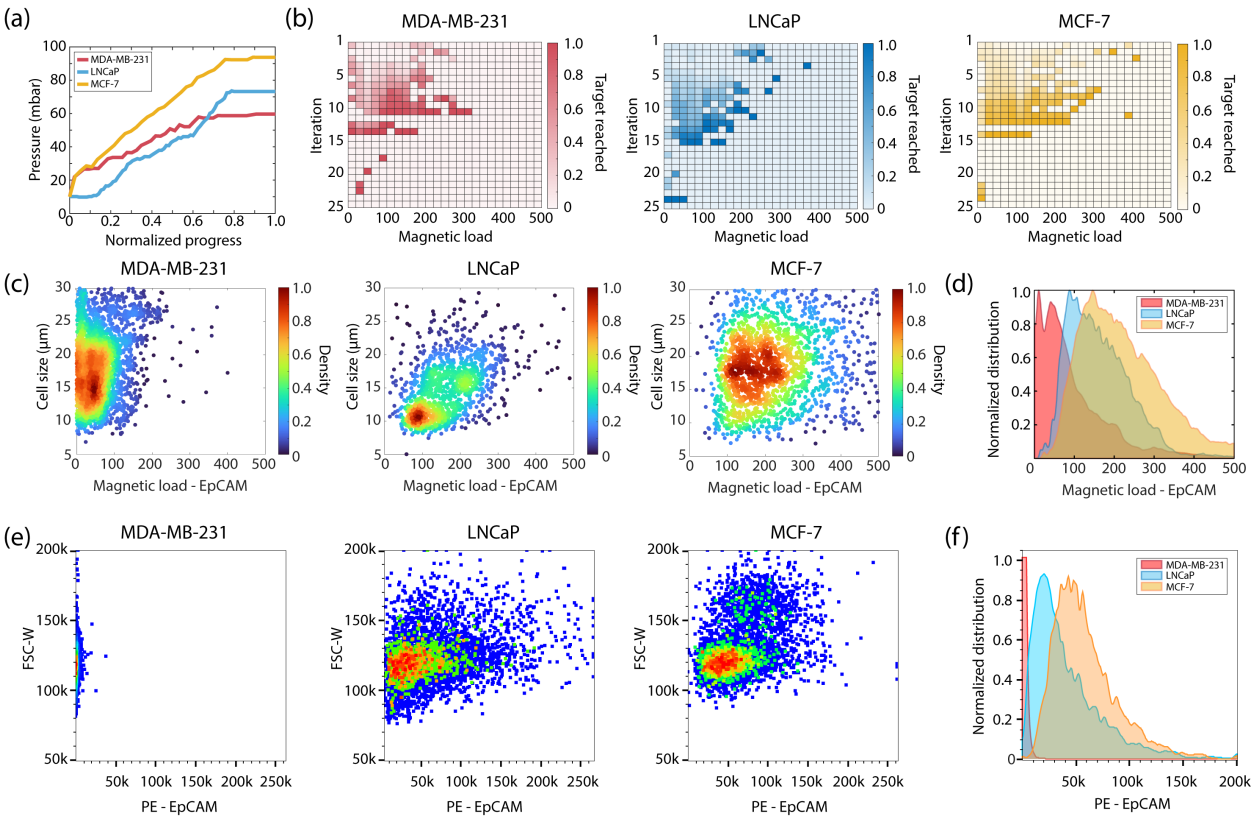

Fig. 4. Analysis of the homogeneous samples with varying surface expression. (a) The results for the boundary pressure analysis. (b) Evolution of the measurement scores per iteration. The algorithm was able to reach all its targets in less than 25 iterations for all 3 cell lines. (c) Scatter plots of magnetic load versus cell size for all cell lines. (d) Histogram of the surface expression acquired with our automated cytometer. (e) Flow cytometry validation of the analysis. (f) Flow cytometry histogram for the surface expression confirmed our surface expression measurements.

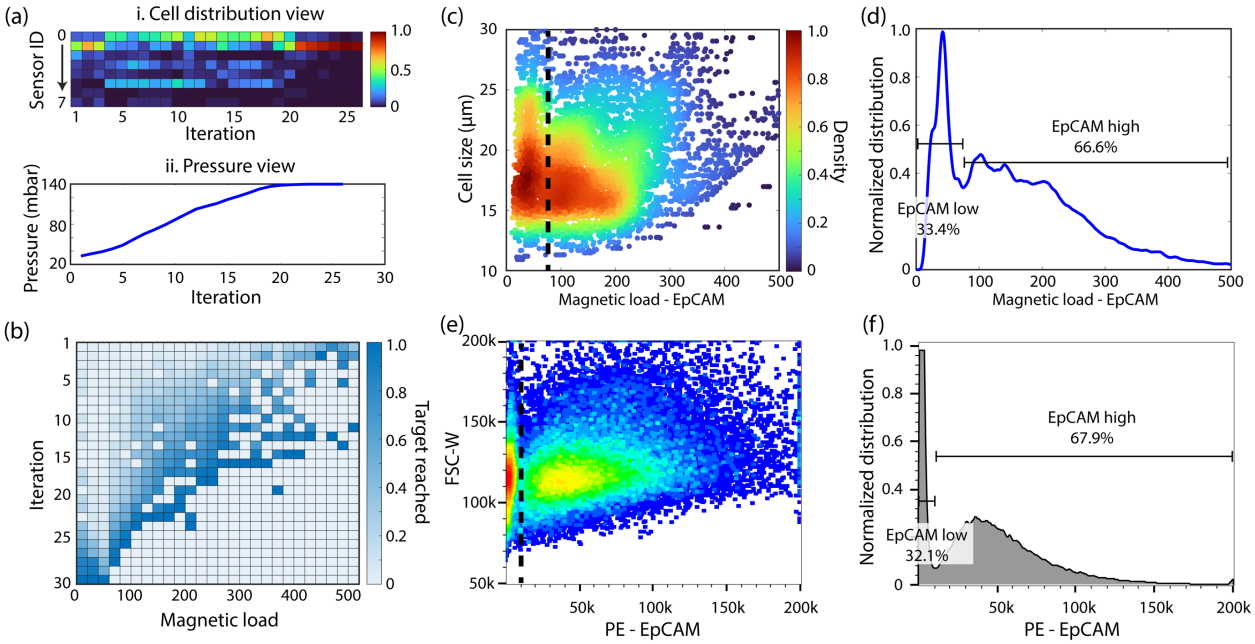

Fig. 5. Analysis of heterogeneous samples. (a) The cell distribution and the evolution of pressure in boundary pressure search. (b) Progression of the measurement scores. (c) Scatter plot the results from the heterogenous sample. The plot demonstrated 2 distinct peaks corresponding to 2 different cell populations. (d) Histogram view of the surface expression showed the population of the higher surface expression corresponded to the 66.6% and the population with the lower expression accounted for 33.4% of the whole sample when gated by their surface expression. (e) Flow cytometry validation of the experimental results. The two distinct population can be gated based on their surface expression. (f) Histogram representation of the surface expression confirms our measurement for the proportion of the populations against each other.

SUPPLEMENTARY INFORMATION

Table S1. Goodness of fit metrics for the magnetic load mappings.

	SSE	R-square	Adj. R-square	RMSE
Sensor 0	63.83	0.9948	0.9942	1.35
Sensor 1	179.7	0.9974	0.9971	2.266
Sensor 2	311.7	0.983	0.9981	2.984
Sensor 3	1618	0.9951	0.9946	6.8
Sensor 4	657.1	0.9987	0.9985	4.333
Sensor 5	3559	0.9943	0.9937	10.08
Sensor 6	1252	0.9982	0.9980	5.98
Sensor 7	1252	0.9982	0.9980	5.98

Table S2. Overall comparison of our approach to fluorescence-based cytometry.

Traits	**Our approach**	**Fluorescence-based cytometry**
Excitation source	Permanent magnet	Laser
Method of action	Physical displacement	Fluorescent intensity
Readout mechanism	Electrical	Optical
Maintenance	Not required	Required for optical components
Operational complexity	No training required	Operator must be specifically trained
User experience	No user input necessary	User must manually set excitation parameters and intensity gain
Portability	High	Usually employed as benchtop device
Dynamic range	~1:500	~1:250,000
Separation capability	Integrated	Possible with an actuator
Potential sources of variation	Between different fabrication batches	Between different users, laboratories, protocols, and optical detectors used in the instrument
Co-expression	No	Yes

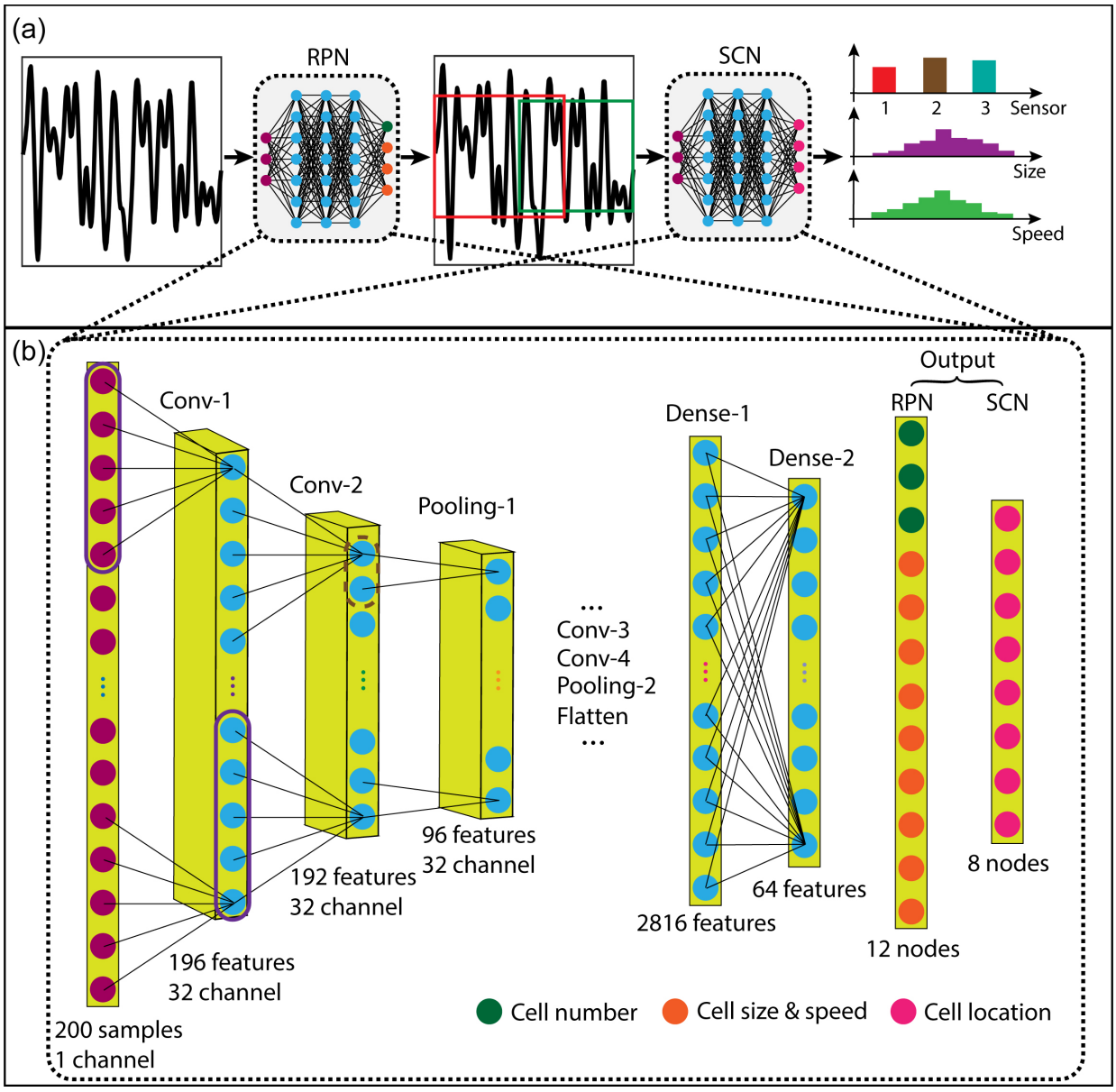

Fig. S1. Deep learning-based signal processing algorithm. (a) Workflow of the two-stage ConvNet model. Given a sensor waveform, the first stage ConvNet, region proposal network (RPN), detects and fits a bounding box on each contained signature waveform. The second stage ConvNet, sensor classification network (SCN), predicts the sensor identity of each identified signature waveform. (b) The network structure of the RPN and SCN. The RPN and SCN share the same structure (4 convolution layers) for feature extraction. The output layer of the RPN has 12 nodes, where the first three nodes represent the number of contained signature waveforms, the rest nine nodes, three in a group, represent the bounding box parameters. The output layer of the SCN has eight nodes, represent eight sensors.

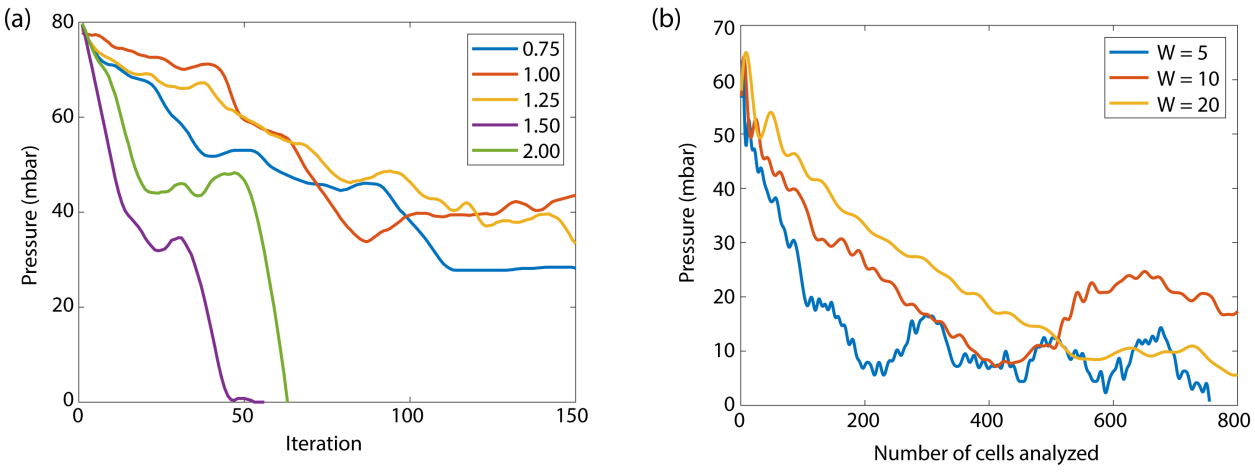

Fig. S2. Optimization of (a) the global gain coefficient and (b) update period. Based on these results, a global gain coefficient of 1.00 and an update period of 20 was chosen for the best results.

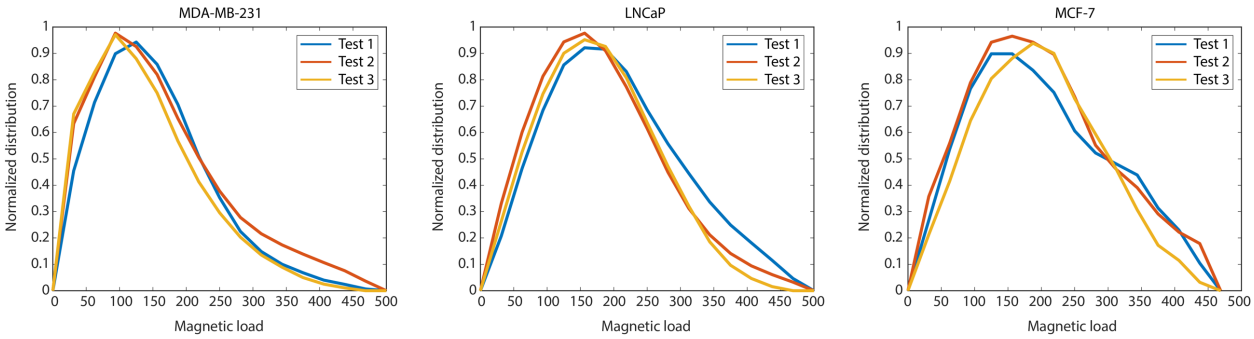

Fig. S3. The surface expression measurements were repeated for 3 times for each cell lines. All the results presented the same magnetic load distribution showing the repeatability of our system.

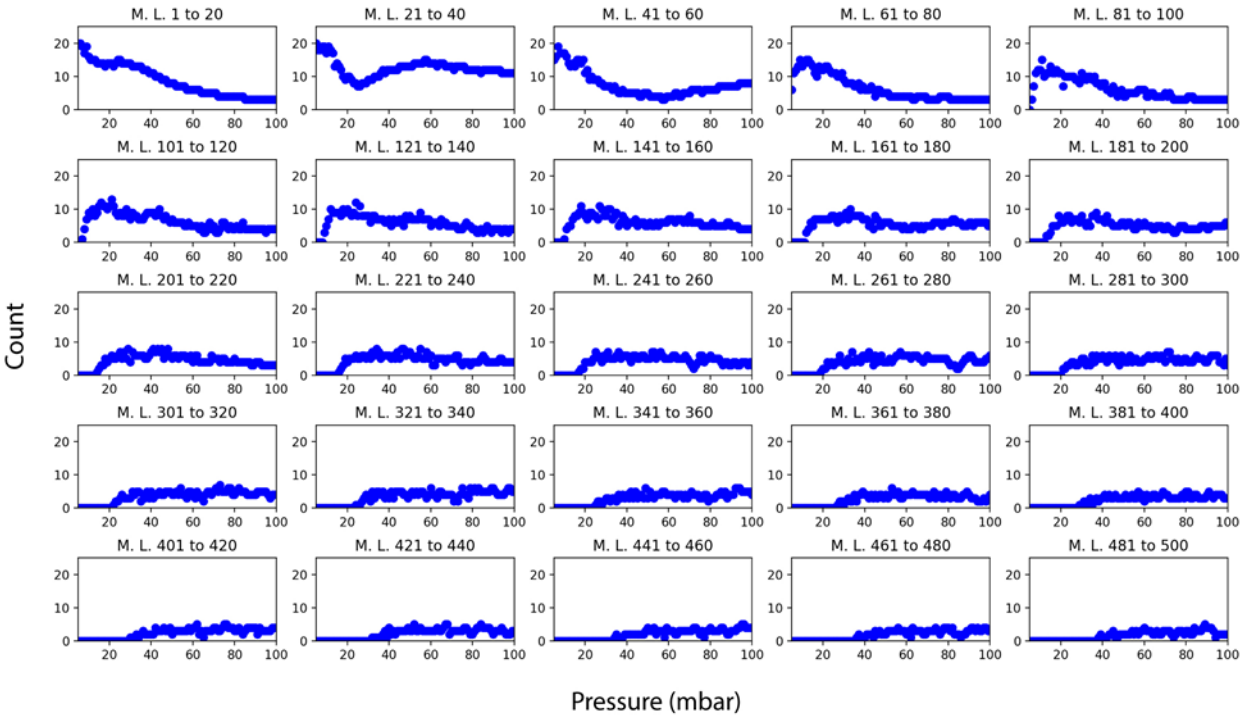

Fig. S4. Number of cells (N) that can be assigned in each magnetic load window given different drive pressures.

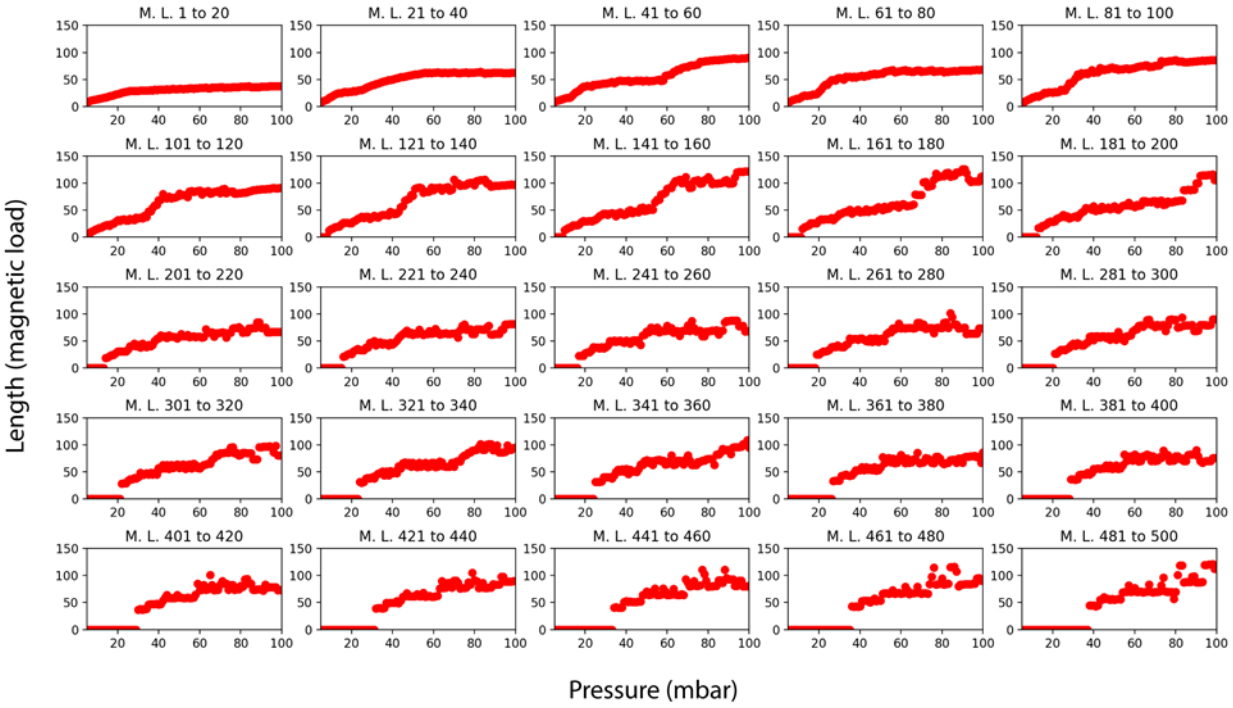

Fig. S5. Mean of spreads in each magnetic load window given different drive pressures.

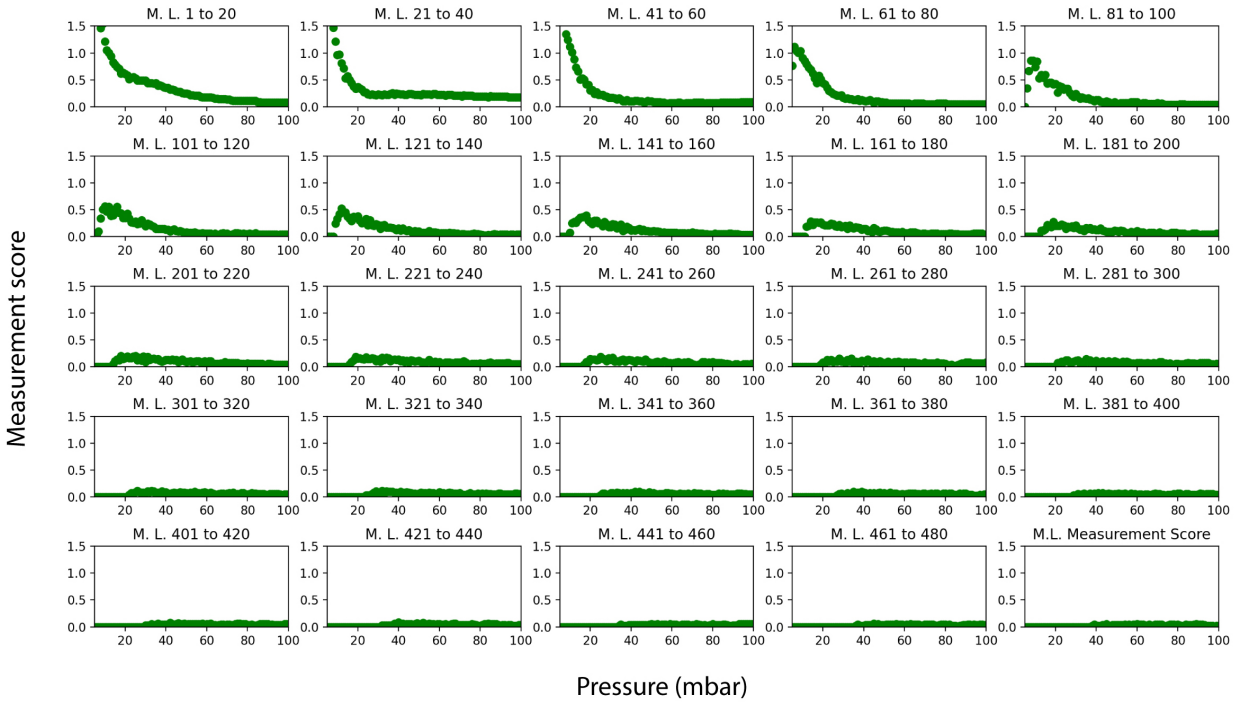

Fig. S6. Measurement score in each magnetic load window given different drive pressures after calculating for feasible cell properties.